

Magnetic and Nematic Orders of the Two-Dimensional Electron Gas at Oxide (111) Surfaces and Interfaces

Nazim Boudjada, Gideon Wachtel, and Arun Paramekanti

Department of Physics, University of Toronto, Toronto, Ontario M5S 1A7, Canada

Recent experiments have explored two-dimensional electron gases (2DEGs) at oxide (111) surfaces and interfaces, finding evidence for hexagonal symmetry breaking in SrTiO₃ at low temperature. We discuss many-body instabilities of such (111) 2DEGs, incorporating multiorbital interactions in the t_{2g} manifold which can induce diverse magnetic and orbital orders. Such broken symmetries may partly account for the observed nematicity, cooperating or competing with phonon mechanisms. We present an effective field theory for the interplay of magnetism and nematic charge order, and discuss implications of the nematicity for transport and superconductivity in (111) 2DEGs.

Introduction.— Transition metal oxide heterostructures and interfaces can realize exotic low-dimensional electronic phases and allow for engineering oxide-based devices [1]. Extensive research [2–13, 15–24] has focused on the two-dimensional electron gas (2DEG) at the (001) LaAlO₃-SrTiO₃ (LAO-STO) interface induced by a combination of the polar catastrophe and oxygen vacancies. This 2DEG shows evidence of correlated magnetism in torque magnetometry and scanning SQUID measurements [10, 11]. In addition, it exhibits superconductivity (SC) [6, 25] which may be tied to that of doped bulk STO, though the interface might harbor modulated SC pairing [26] or Majorana modes [27].

Recently, various groups have started to probe 2DEGs at oxide (111) surfaces and interfaces, for instance induced by photon [28] or ion [29, 30] irradiation at the (111) STO surface, as well as that at the (111) LAO-STO interface [31–35]. Part of this interest stems from proposals for realizing topologically nontrivial phases along this growth direction [36–43]. The [111] growth direction is polar for STO due to alternating Ti⁴⁺ and (SrO₃)⁴⁻ layers, and the internal electric fields could lead to stronger confinement [44] of the (111) 2DEG, potentially enhancing correlation effects relative to (001) 2DEGs. Angle resolved photoemission spectroscopy (ARPES) on the (111) STO surface reveals a Fermi surface (FS) composed of all three t_{2g} orbitals, which appears to preserve the expected hexagonal symmetry [28, 29]. However, very recent experiments have discovered, via measurements of magnetotransport [30–33] and the resistive transition into the SC state [35], that this (111) 2DEG exhibits an anisotropy which sets in at low temperatures, spontaneously breaking the hexagonal symmetry. While a weak resistive anisotropy may arise from the ~ 100 K pseudo-cubic to pseudo-tetragonal transition of bulk STO [45], the onset temperature seen in these experiments is much lower, $T_{\text{ani}} \sim 4\text{--}30$ K depending on the sample and the

electron density. For bulk STO, it is known that the transition into the pseudo-tetragonal phase is sensitive to stress along the [111] direction [46], and proceeds via an intermediate trigonal phase; it remains to be tested if the lower symmetry at the (111) surface or interface leads to a low temperature surface phonon instability.

In light of these developments, it is in any case also important to consider the impact of electron-electron interactions on (111) 2DEGs, in order to (i) study possible interaction induced many-body instabilities, and (ii) ask if there are electronic mechanisms for the observed anisotropies of the (111) 2DEG which may cooperate or compete with phonon instabilities. Such an interplay has been actively investigated in the iron pnictide superconductors (see Ref. 47 for a review).

Motivated by these questions, we examine a model for t_{2g} electronic states of the (111) STO surface 2DEG, which is consistent with the ARPES measurements, and study its instabilities driven by multiorbital interactions. Our main findings, summarized in Figs. 1 and 2, based on a combination of random phase approximation (RPA) calculations supplemented by mean field theory, is that there is a range of densities over which this 2DEG is unstable to ferromagnetic (FM) or antiferromagnetic (AF) order, accompanied by ferro-orbital order. Even if thermal fluctuations melt such magnetic orders in 2D, the orbital order and the fluctuating magnetism are expected to survive to higher temperatures, leading to a nematic fluid [48–53] which breaks hexagonal symmetry. We present a Landau theory of this nematic, and discuss implications for transport measurements and superconductivity. Such nematicity induced by orbital or spin order has been previously considered for the (001) 2DEG [23, 54–56]. Our results should be broadly applicable to a wide class of oxide (111) 2DEGs.

Model.— We begin with a tight-binding model of Ti t_{2g} -orbitals on a 2D triangular lattice which captures the FS seen in ARPES [28, 29] for the (111) 2DEG at

the STO surface:

$$H_0 = \sum_{\mathbf{k}\ell\ell'\sigma} c_{\ell\sigma}^\dagger(\mathbf{k}) h_{\ell\ell'}(\mathbf{k}) c_{\ell'\sigma}(\mathbf{k}) \quad (1)$$

with $\ell \equiv yz, zx, xy$, and

$$\underline{h}(\mathbf{k}) = \begin{pmatrix} \epsilon_{\mathbf{k}}^c + \eta_{\mathbf{k}}^{ab} & \gamma_{\mathbf{k}}^a & \gamma_{\mathbf{k}}^b \\ \gamma_{\mathbf{k}}^a & \epsilon_{\mathbf{k}}^b + \eta_{\mathbf{k}}^{ca} & \gamma_{\mathbf{k}}^c \\ \gamma_{\mathbf{k}}^b & \gamma_{\mathbf{k}}^c & \epsilon_{\mathbf{k}}^c + \eta_{\mathbf{k}}^{bc} \end{pmatrix}, \quad (2)$$

where $\epsilon_{\mathbf{k}}^\alpha = -2t \cos k_\alpha$ and $\eta_{\mathbf{k}}^{\alpha\beta} = -2t_\perp (\cos k_\alpha + \cos k_\beta)$ determine the intraorbital dispersion which leads to elliptical FSs, while $\gamma_{\mathbf{k}}^\alpha = -2t' \cos k_\alpha$ captures weak interorbital hopping. Here, we have defined $k_\alpha = \mathbf{k} \cdot \hat{a}$ ($\alpha = a, b, c$), with $\hat{a} = \hat{x}$, $\hat{b} = \hat{x}/2 + \hat{y}\sqrt{3}/2$, and $\hat{c} = -\hat{x}/2 + \hat{y}\sqrt{3}/2$. We work in units where the triangular lattice constant $d \approx 5.66 \text{ \AA}$ is set to unity. The ARPES data [28, 29] can be reasonably fit by choosing $t = 320 \text{ meV}$ and $t_\perp = 0.04t$, and an electron density of $\bar{n} = 0.3$ electrons per site, corresponding to 10^{14} cm^{-2} ; we therefore study a range of densities around this value. The interorbital terms appear to be small; for concreteness, we set $t' = -0.04t$. The resulting FSs are shown overlaid on the paramagnetic phases in Fig. 2. The real 2DEG wave functions will be spread over a few layers, so H_0 should only be viewed as the simplest 2D tight-binding parameterization of the ARPES data. We omit spin-orbit coupling (SOC), but comment on its effects later. The local multiorbital interactions are

$$H_{\text{int}} = U \sum_{i\ell} n_{i\ell\uparrow} n_{i\ell\downarrow} + \frac{1}{2} V \sum_{i\ell \neq \ell'} n_{i\ell} n_{i\ell'} - J \sum_{i\ell \neq \ell'} \mathbf{S}_{i\ell} \cdot \mathbf{S}_{i\ell'} + J' \sum_{i\ell \neq \ell'} c_{i\ell\uparrow}^\dagger c_{i\ell\downarrow}^\dagger c_{i\ell'\downarrow} c_{i\ell'\uparrow}. \quad (3)$$

where i denotes the site and ℓ the orbital. Below, we fix $V = (U - 5J/2)$ and $J' = J$ as appropriate for t_{2g} orbitals, and explore broken symmetry states driven by varying the interactions $J/t, U/t$. These interactions should be scaled down compared to atomic values by the number of layers over which the 2DEG is spread.

RPA analysis. — To identify the leading weak-coupling instabilities we use an unbiased multi-orbital RPA approach [57], with the matrix response $\underline{\chi}_{RPA}^{(c,s)}(\mathbf{q}, \Omega) = \underline{\chi}_0(\mathbf{q}, \Omega) (1 - \underline{U}^{(c,s)} \underline{\chi}_0(\mathbf{q}, \Omega))^{-1}$, where

$$\left(\underline{\chi}_0(\mathbf{q}, \Omega) \right)_{\ell_1 \ell_2; \ell_3 \ell_4} = \frac{1}{N} \sum_{ij\sigma\sigma'} \int_0^\beta d\tau e^{i\mathbf{q} \cdot (\mathbf{r}_i - \mathbf{r}_j) - i\Omega\tau} \times \left\langle c_{i\ell_1\sigma}^\dagger(\tau) c_{i\ell_2\sigma}(\tau) c_{j\ell_3\sigma'}^\dagger(0) c_{j\ell_4\sigma'}(0) \right\rangle. \quad (4)$$

is the bare response function (see Supplemental Material (SM)). Here, N is the number of sites, c and s respectively denote charge and spin responses. The non-zero

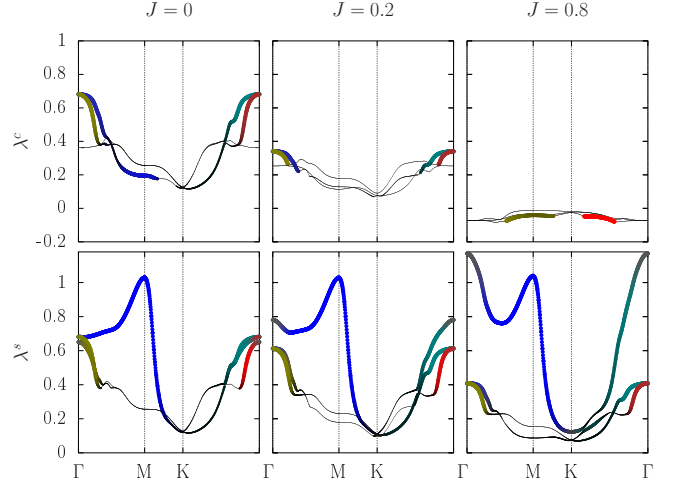


FIG. 1: Dominant three eigenvalues $\lambda^{(c,s)}$ ($c = \text{charge}$, $s = \text{spin}$) of the matrix product $\underline{U}^{(c,s)} \underline{\chi}_0(\mathbf{q}, \Omega = 0)$, plotted along high symmetry lines of the BZ, with $t = 1$, $U = 2$, $t_\perp = -t' = 0.04$, and $T = 0.02$, for fixed density $\bar{n} = 0.3$, and varying Hund's coupling J/t . Line color (red, green, blue) indicates relative weight of orbitals (respectively xy, xz, yz) in the orbital-diagonal part of the eigenvectors $|f_{\ell\ell}^{(c,s)}|^2$; thickness indicates total weight, $\sum_{\ell} |f_{\ell\ell}^{(c,s)}|^2$. The dominant instability is in the spin channel, being antiferromagnetic (near M) for small J and ferromagnetic (at Γ) for large J . In the charge channel, the leading instability at small J is a two-fold degenerate mode at Γ corresponding to ferro-orbital order.

interaction vertex matrices are,

$$\begin{aligned} (U^c)_{\ell\ell;\ell\ell} &= -U, & (U^c)_{\ell\ell';\ell\ell'} &= -2V, \\ (U^c)_{\ell\ell';\ell'\ell'} &= V - \frac{3}{2}J, & (U^c)_{\ell\ell';\ell'\ell} &= -2J', \end{aligned} \quad (5)$$

$$\begin{aligned} (U^s)_{\ell\ell;\ell\ell} &= U, & (U^s)_{\ell\ell';\ell'\ell'} &= J, \\ (U^s)_{\ell\ell';\ell'\ell'} &= \frac{1}{2}J - V, & (U^s)_{\ell\ell';\ell'\ell} &= 2J', \end{aligned} \quad (6)$$

where $\ell \neq \ell'$. When the largest eigenvalue of $\underline{U}^{(c,s)} \underline{\chi}_0(\mathbf{q}, \Omega = 0)$ is $\lambda^{(c,s)}(\mathbf{q}) = 1$, the response function diverges, indicating an instability towards an ordered state, with corresponding eigenvectors, $f_{\ell\ell'}^{(c,s)}(\mathbf{q})$. Figure 1 shows the largest eigenvalues, $\lambda^c(\mathbf{q})$ and $\lambda^s(\mathbf{q})$ along high symmetry lines in the Brillouin zone (BZ) for $\bar{n} = 0.3$, $U/t = 2$ and temperature $T/t = 0.02$, demonstrating the emergence of various instabilities as we vary Hund's coupling. For our choice of experimentally motivated parameters, the leading instabilities are nearly orbital diagonal, $f_{\ell\ell'}^{(c,s)}(\mathbf{q}) \approx f_{\ell}^{(c,s)}(\mathbf{q}) \delta_{\ell\ell'}$.

When $J = 0$, the Hubbard interaction U drives a leading instability in the spin channel, with \mathbf{q} generically

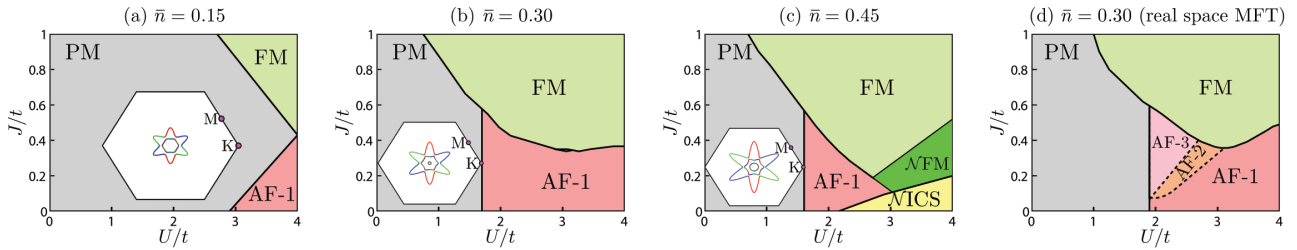


FIG. 2: Zero temperature phase diagram of the (111) 2DEG as a function of the Hubbard repulsion U/t and Hund's coupling J/t for densities (a) $\bar{n} = 0.15$, (b) $\bar{n} = 0.30$, (c) $\bar{n} = 0.45$ within a single- \mathbf{Q} spiral mean field theory (MFT). The different metallic phases are paramagnetic phase (PM), stripe antiferromagnet (AF-1), incommensurate spiral (ICS), and a ferromagnetic phase (FM) at large Hund's coupling. The PM phases depict the noninteracting Fermi surfaces. (d) Real space MFT (at $\bar{n} = 0.3$, $T = 0.02t$) showing that the commensurate AF might support regimes of multi- \mathbf{Q} orders (AF-2, AF-3). The \mathcal{N} FM, ICS, AF-1, and AF-2 phases coexist with ferro-orbital order which will lead to transport anisotropies.

incommensurate (close to the M points of the BZ for the range of densities investigated), with all the weight on a single orbital. This instability indicates a tendency towards incommensurate spiral or commensurate stripe antiferromagnetic (AF) order – for each orbital in a different direction. In the charge channel, we find a sub-leading instability, with two degenerate eigenvalues at $\mathbf{q} = 0$, indicating a tendency towards ferro-orbital order which will lead to nematicity associated with broken lattice rotational symmetry. With increasing J , the AF instability gives way to a ferromagnetic (FM) instability seen in the spin response at the Γ -point. At the same time, the ferro-orbital response is strongly suppressed. Below, we use mean field theory (MFT) in order to further characterize the broken symmetry phases.

Mean field theory. — We study the phase diagram of our model, Eqns. (1)-(3), using a momentum space MFT within a single- \mathbf{Q} spiral ansatz with a spatially uniform but orbital-dependent density. This is captured by a mean field Hamiltonian, $H_{\text{var}} = H_0 - \sum_{i\ell} (\phi_\ell + \mu) n_{i\ell} - \sum_{i\ell} \mathbf{b}_\ell \cdot \mathbf{S}_{i\ell} e^{i\mathbf{Q} \cdot \mathbf{r}_i}$, which we use to generate variational ground states $|\psi_{\text{var}}\rangle$ at the desired charge density by tuning μ . The fields ϕ_ℓ , \mathbf{b}_ℓ , and the wavevector \mathbf{Q} are selected to minimize $\langle \psi_{\text{var}} | H_0 + H_{\text{int}} | \psi_{\text{var}} \rangle$ (see SM).

Fig. 2 (a)-(c) shows the MFT phase diagrams for densities $\bar{n} = 0.15, 0.30, 0.45$. Broadly, we find three phases consistent with RPA: (i) a paramagnetic (PM) metal where $\phi_\ell = 0$, $\mathbf{b}_\ell = 0$, (ii) a commensurate stripe-AF (AF-1) or incommensurate spiral (ICS) metal driven by U , where $\phi_\ell \neq 0$ and $\mathbf{b}_\ell \neq 0$, which has higher density in one of the three orbitals, and (iii) a FM metal driven by Hund's coupling where $\mathbf{b}_\ell = \mathbf{b}$, and $\mathbf{Q} = 0$, either having the same density in all orbitals (FM), or

with one orbital having a lower density than the other two (i.e., a nematic FM: \mathcal{N} FM). Interestingly, we find a direct (generically first-order) transition from the PM into the AF-1 phase for all three densities, in contrast to the RPA which finds AF-1 only at a fine-tuned density.

To go beyond the single- \mathbf{Q} ansatz, we have also studied the commensurate AF by minimizing the free energy at $T = 0.02t$ assuming a 2×2 unit cell. The result for $\bar{n} = 0.3$ is shown in Fig. 2(d) (see also SM); we find reasonably good agreement with the single- \mathbf{Q} MFT, but discover small regimes where the single- \mathbf{Q} order gives way to multi- \mathbf{Q} condensates where two (AF-2) or three (AF-3) wavevectors are simultaneously present. A robust feature is the presence of simultaneous AF and ferro-orbital order in the AF-1 and AF-2 phases. A similar competition between single- \mathbf{Q} and multi- \mathbf{Q} phases also appears in single-orbital honeycomb and triangular lattice Hubbard models [5, 59].

The \mathcal{N} FM, AF-1, AF-2, and ICS phases feature discrete ferro-orbital order which breaks the hexagonal lattice symmetry. Thus, even if fluctuations melt the magnetic order itself, there may be large regimes in the phase diagram where the electronic nematicity survives. Below we use Landau theory to further understand this interplay of magnetism and nematicity.

Effective field theory. — Landau theory is a powerful tool to analyze magnetic orders [17] and study spin textures such as skyrmions which might arise at the (001) LAO-STO interface [56]. For the (111) 2DEG, our RPA analysis suggests that the soft electronic modes include a complex nematic charge mode $\psi_n = \delta\rho_{xy} + \omega\delta\rho_{yz} + \omega^2\delta\rho_{zx}$ (with $\omega = e^{i2\pi/3}$) constructed from the slowly varying orbital densities $\delta\rho_\ell$ at the Γ -point, and the spin modes, $\vec{\varphi}_0$ at the Γ -point, and

$\vec{\varphi}_\alpha$ at the magnetic wavevectors \mathbf{Q}_α ($\alpha = 1, 2, 3$), which can describe both FM and AF orders. Since the interorbital hopping is small, $\vec{\varphi}_{1,2,3} \sim \vec{\varphi}_{xy,yz,zx}$ but with weak orbital admixture. The spin modes $\vec{\varphi}_\alpha$ are complex for incommensurate \mathbf{Q}_α , and real if \mathbf{Q}_α correspond to the commensurate M -points. The nematic order parameter ψ_n transforms under anticlockwise lattice $\pi/3$ -rotations as $\psi_n \rightarrow \omega^2 \psi_n$, and under reflections about the \hat{x} -axis as $\psi_n \rightarrow \psi_n^*$. Turning to the spin modes, $\vec{\varphi}_0$ is invariant under lattice symmetries, anticlockwise $\pi/3$ -rotations leads to $\vec{\varphi}_1 \rightarrow \vec{\varphi}_2, \vec{\varphi}_2 \rightarrow \vec{\varphi}_3, \vec{\varphi}_3 \rightarrow \vec{\varphi}_1^*$. Under spin rotations, ψ_n is invariant but all spin modes undergo $SO(3)$ rotations, $\vec{\varphi}_{0,\alpha} \rightarrow \mathfrak{R} \vec{\varphi}_{0,\alpha}$. Time-reversal sends $\vec{\varphi}_{0,\alpha} \rightarrow -\vec{\varphi}_{0,\alpha}$. Armed with this, the mean field Landau free energy is $\mathcal{F} = \int d^2x (\mathcal{L}_\psi + \mathcal{L}_\varphi + \mathcal{L}_{\psi\varphi})$, with

$$\mathcal{L}_\psi = r_\psi |\psi_n|^2 + w_\psi (\psi_n^3 + \psi_n^{*3}) + u_\psi |\psi_n|^4 + \dots \quad (7)$$

$$\mathcal{L}_\varphi = r_0 \vec{\varphi}_0 \cdot \vec{\varphi}_0 + r_Q \sum_\alpha |\vec{\varphi}_\alpha|^2 + \dots \quad (8)$$

$$\mathcal{L}_{\psi\varphi} = -\lambda_1 (\psi_n^* \mathcal{S}_n + \psi_n \mathcal{S}_n^*) - \lambda_2 |\vec{\varphi}_0|^2 |\psi_n|^2, \quad (9)$$

where we have defined a complex magnetic nematic order $\mathcal{S}_n = |\vec{\varphi}_1|^2 + \omega |\vec{\varphi}_2|^2 + \omega^2 |\vec{\varphi}_3|^2$ which transforms analogous to ψ_n . In this effective field theory, the PM phase corresponds to ($r_\psi, r_0, r_Q > 0$), the FM phase corresponds to ($r_0 < 0, r_\psi, r_Q > 0$), and the various AF phases correspond to ($r_Q < 0, r_0 > 0$). Note that we never find a ground state nematic charge order unaccompanied by spin order in the MFT. The various types of AF orders will be dictated by higher order (quartic and sixth order) terms denoted above by ellipsis. In turn, this can lead to a ‘pinning field’ for the charge nematic order via the cubic interaction λ_1 in $\mathcal{L}_{\psi\varphi}$; our mean field results indicate $w_\psi, \lambda_1, \lambda_2 > 0$. Below, we discuss some implications of this Landau theory, deferring its microscopic derivation to a future publication.

(a) Incommensurate spiral (ICS): For the generic incommensurate instability, the simplest spin order (which will not lead to any charge modulation) is a single-mode coplanar spiral at one \mathbf{Q}_α , with the complex $\vec{\varphi}_\alpha = \hat{\Omega}_1 + i\hat{\Omega}_2$ and $\hat{\Omega}_1 \cdot \hat{\Omega}_2 = 0$. This leads to $\mathcal{S}_n \sim \omega^{\alpha-1}$, so the cubic interaction $\lambda_1 > 0$ will pin $\psi_n \sim \omega^{\alpha-1}$, causing density enhancement in orbital α .

(b) Commensurate AF: For commensurate stripe AF, $\mathbf{Q}_\alpha \equiv M_\alpha$, in which case $\vec{\varphi}_\alpha$ are real fields. This case, for which we have also carried out a real space MFT, leads to three orders. (i) AF-1 has condensation at a single M_α , which corresponds to a collinear stripe order with $\vec{\varphi}_\alpha \sim \hat{\Omega}_1$. This has $\mathcal{S}_n \sim \omega^{\alpha-1}$, which pins $\psi_n \sim \omega^{\alpha-1}$, leading to a charge nematic order similar to the ICS state. (ii) AF-2 features condensation at a pair of wavevectors M_α, M_β , with $\langle \vec{\varphi}_\alpha \rangle \sim \hat{\Omega}_1$

and $\langle \vec{\varphi}_\beta \rangle \sim \hat{\Omega}_2$. This state can be either collinear, $\hat{\Omega}_1 = \hat{\Omega}_2$, or coplanar, $\hat{\Omega}_1 \cdot \hat{\Omega}_2 = 0$. In both case, however, $\mathcal{S}_n, \psi_n \sim \omega^{\alpha-1} + \omega^{\beta-1}$, displaying charge nematic order. (iii) Finally, AF-3 is a triple- \mathbf{Q} spin crystal, similarly featuring either collinear or non-coplanar tetrahedral order of the spins. Both cases are obtained by condensation at all three M -points, with $\langle \vec{\varphi}_{1,2,3} \rangle \sim \hat{\Omega}_{1,2,3}$, and $\mathcal{S}_n = 0$, so no charge nematic is induced. In the collinear case $\hat{\Omega}_1 = \hat{\Omega}_2 = \hat{\Omega}_3$, while in the non-coplanar spin order $\hat{\Omega}_1 \cdot \hat{\Omega}_2 = 0$, and $\hat{\Omega}_3 = \pm \hat{\Omega}_1 \times \hat{\Omega}_2$. The latter case, in the presence of interorbital hopping, will feature an anomalous Hall effect [61, 62]. The collinear AF-2 and AF-3 will also break translational symmetries with associated charge modulation driven by terms proportional to $\vec{\varphi}_\alpha \cdot \vec{\varphi}_\beta \neq 0$; such orders may be favored by repulsive interactions between neighboring sites.

(c) Nematic FM (NFM): Starting with a uniform FM state, the quartic coupling $\lambda_2 > 0$, if sufficiently large, can drive charge nematicity, since it can change the ‘mass’ of the nematic field to ($r_\psi - \lambda_2 |\vec{\varphi}_0|^2$). This coupling between FM and nematic orders is not linear in ψ_n , unlike the above AFM/ICS cases. Thus, the nematicity in this case is not symmetry-enforced. For $w_\psi > 0$, the NFM will have depletion of the density in one orbital, as we find from the MFT.

Fluctuation/disorder effects. — In 2D, without SOC, thermal fluctuations will destroy long-range magnetic order at any $T > 0$. In this case, ICS, the NFM, the collinear AF-1, and orthogonal AF-2, will melt into a charge nematic, reflected in a nonzero ψ_n, \mathcal{S}_n , which will undergo symmetry restoration via a Z_3 clock (or 3-state Potts) transition. Within MFT this is a first order transition, but thermal fluctuations render it a continuous transition [63]. The non-coplanar AF-3 state will lead to a magnetically melted state with only chiral order (linked to the \pm choice of $\hat{\Omega}_3$), featuring a nonzero anomalous Hall effect that vanishes above an Ising transition at which time-reversal symmetry is restored [62].

We speculate that disorder might also weakly suppress long-range magnetic order, even with SOC, leaving vestigial nematic order [64] down to $T = 0$. This suggestion is motivated by $\text{Sr}_3\text{Ru}_2\text{O}_7$, where the observation of nematic transport [65] near the metamagnetic critical point was recently attributed, via neutron scattering, to arise from *nearly* ordered SDW phases [66].

Discussion. — The electronic nematic phases we have proposed in (111) 2DEGs will lead to transport anisotropies. On symmetry grounds, the scaled resistive anisotropy $(\rho_{xx} - \rho_{yy})/(\rho_{xx} + \rho_{yy})$ will track the nematic order parameter [67, 68]. A simple Drude picture (see SM) shows that, for the coordinates used above, $\rho_{xx} - \rho_{yy} \sim \text{Re } \psi$ while $\rho_{xy} = \rho_{yx} \sim \text{Im } \psi$. Further signa-

tures of nematic order may be observed in Friedel oscillations which can be probed using scanning tunneling spectroscopy. Even in a conventional phonon-induced SC state, the presence of such background nematic order would lead to an anisotropy of the vortex shape and the mobility as well as the critical current, explaining the anisotropy observed in the resistive transition into the SC state [35]. If such orbital order is weak, it will be less evident in ARPES [28, 29] than in transport probes.

Rashba SOC [1–4] does not significantly impact the (111) FS for relevant densities $\bar{n} \sim 0.3$, or lead to a significant spin-splitting near the tips of the elliptical FSs where we find the magnetic instability (see SM) since orbital mixing is negligible at those momenta. Thus, we expect SOC will not significantly modify the phase diagram at these densities; however, it can pin the magnetic order or convert the uniform FM into a long wavelength spiral [17, 56]. SOC will have a more significant impact on low density 2DEGs, and transport properties which average over the entire FS of all bands.

Our work has not taken into account random oxygen vacancies - these can locally pin the nematic order but cannot induce anisotropies in macroscopically averaged resistivity measurements. However, such ‘nematogen’ defects could amplify weak resistive anisotropies, both of the bulk tetragonal phase in dilute 2DEGs, as well as of the higher density nematic phases with orbital order. This interplay, which has been studied in the pnictides [72], would be worth exploring in the oxide 2DEGs.

Finally, tetragonal lattice distortions, described by a 3-state Potts theory [45] similar to \mathcal{L}_ψ , will couple linearly to the nematic order parameter ψ_n itself, affecting the SDW degrees of freedom as well. For instance, a tetragonal distortion with elongation of the c -axis will favor the nematic order associated with the AF-1 state. The interplay of electronic nematicity explored here, with anisotropies induced by surface phonon mechanisms, is an important topic for future research.

We thank F. Y. Bruno, Q. Li, L. Miao, A. Chubukov, and E. Fradkin for useful discussions and feedback. This research was supported by NSERC of Canada. AP acknowledges the support and hospitality of the International Center for Theoretical Sciences (Bangalore) during completion of this manuscript.

[1] Jak Chakhalian, John W. Freeland, Andrew J. Millis, Christos Panagopoulos, and James M. Rondinelli, “Colloquium,” *Rev. Mod. Phys.* **86**, 1189–1202 (2014).
 [2] A. Ohtomo and H.Y. Hwang, “A high-mobility electron

gas at the LaAlO₃/SrTiO₃ heterointerface,” *Nature* **427**, 423–426 (2004).
 [3] S. Thiel, G. Hammerl, A. Schmehl, C. W. Schneider, and J. Mannhart, “Tunable Quasi-Two-Dimensional Electron Gases in Oxide Heterostructures,” *Science* **313**, 1942–1945 (2006).
 [4] Naoyuki Nakagawa, Harold Y Hwang, and David A Muller, “Why some interfaces cannot be sharp,” *Nature materials* **5**, 204–209 (2006).
 [5] M. Takizawa, H. Wadati, K. Tanaka, M. Hashimoto, T. Yoshida, A. Fujimori, A. Chikamatsu, H. Kumigashira, M. Oshima, K. Shibuya, T. Mihara, T. Ohnishi, M. Lippmaa, M. Kawasaki, H. Koinuma, S. Okamoto, and A. J. Millis, “Photoemission from Buried Interfaces in LaAlO₃/SrTiO₃ Superlattices,” *Phys. Rev. Lett.* **97**, 057601 (2006).
 [6] N. Reyren, S. Thiel, A. D. Caviglia, L. Fitting Kourkoutis, G. Hammerl, C. Richter, C. W. Schneider, T. Kopp, A.-S. Rüetschi, D. Jaccard, M. Gabay, D. A. Muller, J.-M. Triscone, and J. Mannhart, “Superconducting interfaces between insulating oxides,” *Science* **317**, 1196–1199 (2007).
 [7] AD Caviglia, Stefano Gariglio, Nicolas Reyren, Didier Jaccard, T Schneider, M Gabay, S Thiel, G Hammerl, Jochen Mannhart, and J-M Triscone, “Electric field control of the LaAlO₃/SrTiO₃ interface ground state,” *Nature* **456**, 624–627 (2008).
 [8] A. D. Caviglia, M. Gabay, S. Gariglio, N. Reyren, C. Cancellieri, and J.-M. Triscone, “Tunable Rashba Spin-Orbit Interaction at Oxide Interfaces,” *Phys. Rev. Lett.* **104**, 126803 (2010).
 [9] Ariando, X. Wang, G. Baskaran, Z. Q. Liu, J. Huijben, J. B. Yi, A. Annadi, A. Roy Barman, A. Ruydy, S. Dhar, Y. P. Feng, J. Ding, H. Hilgenkamp, and T. Venkatesan, “Electronic phase separation at the LaAlO₃/SrTiO₃ interface,” *Nature Communications* **2**, 188 (2011).
 [10] Julie A Bert, Beena Kalisky, Christopher Bell, Minu Kim, Yasuyuki Hikita, Harold Y Hwang, and Kathryn A Moler, “Direct imaging of the coexistence of ferromagnetism and superconductivity at the LaAlO₃/SrTiO₃ interface,” *Nature physics* **7**, 767–771 (2011).
 [11] Lu Li, C Richter, J Mannhart, and RC Ashoori, “Coexistence of magnetic order and two-dimensional superconductivity at LaAlO₃/SrTiO₃ interfaces,” *Nature physics* **7**, 762–766 (2011).
 [12] Guru Khalsa and A. H. MacDonald, “Theory of the SrTiO₃ surface state two-dimensional electron gas,” *Phys. Rev. B* **86**, 125121 (2012).
 [13] MM Mehta, DA Dikin, CW Bark, S Ryu, CM Folkman, CB Eom, and V Chandrasekhar, “Evidence for charge-vortex duality at the LaAlO₃/SrTiO₃ interface,” *Nature Communications* **3**, 955 (2012).
 [4] Zhicheng Zhong, Anna Tóth, and Karsten Held, “Theory of spin-orbit coupling at LaAlO₃/SrTiO₃ interfaces and SrTiO₃ surfaces,” *Phys. Rev. B* **87**, 161102 (2013).
 [15] Mark H. Fischer, Srinivas Raghu, and Eun-Ah Kim, “Spin-orbit coupling in LaAlO₃/SrTiO₃ interfaces: magnetism and orbital ordering,” *New J. Phys.* **15**, 023022 (2013).

- [16] Younghyun Kim, Roman M. Lutchyn, and Chetan Nayak, “Origin and transport signatures of spin-orbit interactions in one- and two-dimensional SrTiO₃-based heterostructures,” *Phys. Rev. B* **87**, 245121 (2013).
- [17] Sumilan Banerjee, Onur Erten, and Mohit Randeria, “Ferromagnetic exchange, spin-orbit coupling and spiral magnetism at the LaAlO₃/SrTiO₃ interface,” *Nature physics* **9**, 626–630 (2013).
- [18] Gang Chen and Leon Balents, “Ferromagnetism in itinerant two-dimensional t_{2g} systems,” *Phys. Rev. Lett.* **110**, 206401 (2013).
- [19] Se Young Park and Andrew J. Millis, “Charge density distribution and optical response of the LaAlO₃/SrTiO₃ interface,” *Phys. Rev. B* **87**, 205145 (2013).
- [20] Jonathan Ruhman, Arjun Joshua, Shahal Ilani, and Ehud Altman, “Competition Between Kondo Screening and Magnetism at the LaAlO₃/SrTiO₃ Interface,” *Phys. Rev. B* **90** (2014), 10.1103/PhysRevB.90.125123, arXiv:1311.4541.
- [21] M. Diez, A. M. R. V. L. Monteiro, G. Mattoni, E. Cobanera, T. Hyart, E. Mulazimoglu, N. Bovenzi, C. W. J. Beenakker, and A. D. Caviglia, “Giant Negative Magnetoresistance Driven by Spin-Orbit Coupling at the LaAlO₃/SrTiO₃ Interface,” *Phys. Rev. Lett.* **115**, 016803 (2015).
- [22] S. Nandy, N. Mohanta, S. Acharya, and A. Taraphder, “Anomalous transport near the Lifshitz transition at the LaAlO₃/SrTiO₃ interface,” *Phys. Rev. B* **94**, 155103 (2016).
- [23] John R. Tolsma, Marco Polini, and Allan H. MacDonald, “Orbital and spin order in oxide two-dimensional electron gases,” arXiv:1608.03625 [cond-mat] (2016), arXiv:1608.03625.
- [24] W. A. Atkinson, P. Lafleur, and A. Raslan, “Influence of the ferroelectric quantum critical point on SrTiO₃ interfaces,” *Phys. Rev. B* **95**, 054107 (2017).
- [25] D. A. Dikin, M. Mehta, C. W. Bark, C. M. Folkman, C. B. Eom, and V. Chandrasekhar, “Coexistence of superconductivity and ferromagnetism in two dimensions,” *Phys. Rev. Lett.* **107**, 056802 (2011).
- [26] Karen Michaeli, Andrew C. Potter, and Patrick A. Lee, “Superconducting and ferromagnetic phases in SrTiO₃/LaAlO₃ oxide interface structures: Possibility of finite momentum pairing,” *Phys. Rev. Lett.* **108**, 117003 (2012).
- [27] Lukasz Fidkowski, Hong-Chen Jiang, Roman M. Lutchyn, and Chetan Nayak, “Magnetic and superconducting ordering in one-dimensional nanostructures at the LaAlO₃/SrTiO₃ interface,” *Phys. Rev. B* **87**, 014436 (2013).
- [28] T.C. Rödel, C. Bareille, F. Fortuna, C. Baumier, F. Bertran, P. Le Fèvre, M. Gabay, O. Hijano Cubelos, M.J. Rozenberg, T. Maroutian, P. Lecoeur, and A.F. Santander-Syro, “Orientational Tuning of the Fermi Sea of Confined Electrons at the SrTiO₃ (110) and (111) Surfaces,” *Phys. Rev. Applied* **1**, 051002 (2014).
- [29] S. McKeown Walker, A. de la Torre, F.Y. Bruno, A. Tamai, T.K. Kim, M. Hoesch, M. Shi, M.S. Bahramy, P.D.C. King, and F. Baumberger, “Control of a Two-Dimensional Electron Gas on SrTiO₃ (111) by Atomic Oxygen,” *Phys. Rev. Lett.* **113**, 177601 (2014).
- [30] Ludi Miao, Renzhong Du, Yuewei Yin, and Qi Li, “Anisotropic magneto-transport properties of electron gases at SrTiO₃ (111) and (110) surfaces,” *Appl. Phys. Lett.* **109**, 261604 (2016).
- [31] P. K. Rout, I. Agireen, E. Maniv, M. Goldstein, and Y. Dagan, “Six-fold crystalline anisotropic magnetoresistance in (111) LaAlO₃/SrTiO₃ oxide interface,” arXiv:1701.02153 [cond-mat] (2017), arXiv:1701.02153.
- [32] S. Davis, V. Chandrasekhar, Z. Huang, K. Han, Ariando, and T. Venkatesan, “Anisotropic multicarrier transport at the (111) LaAlO₃/SrTiO₃ interface,” *Phys. Rev. B* **95**, 035127 (2017).
- [33] Samuel Kenneth Davis, Zhen Huang, Kun Han, Ariando, Thirumalai Venkatesan, and Venkat Chandrasekhar, “Electrical transport anisotropy controlled by oxygen vacancy concentration in (111) LaAlO₃/SrTiO₃ interface structures,” *Advanced Materials Interfaces* **4**, 1600830 (2017).
- [34] A. M. R. V. L. Monteiro, D. J. Groenendijk, I. Groen, J. de Bruijckere, R. Gaudenzi, H. S. J. van der Zant, and A. D. Caviglia, “Two-dimensional superconductivity at the (111) LaAlO₃/SrTiO₃ interface,” arXiv:1703.04742 [cond-mat] (2017), arXiv:1703.04742.
- [35] S. Davis, Z. Huang, K. Han, Ariando, T. Venkatesan, and V. Chandrasekhar, “Superconductivity and Frozen Electronic States at the (111) LaAlO₃/SrTiO₃ Interface,” arXiv:1704.01203 [cond-mat] (2017), arXiv:1704.01203.
- [36] Di Xiao, Wenguang Zhu, Ying Ran, Naoto Nagaosa, and Satoshi Okamoto, “Interface engineering of quantum hall effects in digital transition metal oxide heterostructures,” *Nat. Comm.* **2**, 596 EP – (2011).
- [37] Andreas Rüegg and Gregory A. Fiete, “Topological insulators from complex orbital order in transition-metal oxides heterostructures,” *Phys. Rev. B* **84**, 201103 (2011).
- [38] Ashley M. Cook and Arun Paramakanti, “Double perovskite heterostructures: Magnetism, Chern bands, and Chern insulators,” *Phys. Rev. Lett.* **113**, 077203 (2014).
- [39] Satoshi Okamoto, Wenguang Zhu, Yusuke Nomura, Ryotaro Arita, Di Xiao, and Naoto Nagaosa, “Correlation effects in (111) bilayers of perovskite transition-metal oxides,” *Phys. Rev. B* **89**, 195121 (2014).
- [40] Xiang Hu, Zhicheng Zhong, and Gregory A. Fiete, “First principles prediction of topological phases in thin films of pyrochlore iridates,” *Sci. Rep.* **5**, 11072 EP – (2015).
- [41] Santu Baidya, Umesh V. Waghmare, Arun Paramakanti, and Tanusri Saha-Dasgupta, “High-temperature large-gap quantum anomalous Hall insulating state in ultrathin double perovskite films,” *Phys. Rev. B* **94**, 155405 (2016).
- [42] L. Si, O. Janson, G. Li, Z. Zhong, Z. Liao, G. Koster, and K. Held, “Quantum anomalous Hall state in ferromagnetic SrRuO₃ (111) bilayers,” ArXiv e-prints (2016), arXiv:1610.01948 [cond-mat.str-el].
- [43] Heung-Sik Kim and Hae-Young Kee, “Realizing Hal-

- dane model in Fe-based honeycomb ferromagnetic insulators,” *npj Quantum Materials* **2**, 20 (2017).
- [44] Santu Baidya, Umesh V. Waghmare, Arun Paramakanti, and Tanusri Saha-Dasgupta, “Controlled confinement of half-metallic two-dimensional electron gas in $\text{BaTiO}_3/\text{Ba}_2\text{FeReO}_6/\text{BaTiO}_3$ heterostructures: A first-principles study,” *Phys. Rev. B* **92**, 161106 (2015).
- [45] Amnon Aharony, K. A. Müller, and W. Berlinger, “Trigonal-to-Tetragonal Transition in Stressed SrTiO_3 : A Realization of the Three-State Potts Model,” *Phys. Rev. Lett.* **38**, 33–36 (1977).
- [46] K. Alex Müller, W. Berlinger, and E. Tosatti, “Indication for a novel phase in the quantum paraelectric regime of SrTiO_3 ,” *Z. Physik B - Condensed Matter* **84**, 277–283 (1991).
- [47] R. M. Fernandes, A. V. Chubukov, and J. Schmalian, “What drives nematic order in iron-based superconductors?” *Nat Phys* **10**, 97–104 (2014).
- [48] Vadim Oganesyan, Steven A. Kivelson, and Eduardo Fradkin, “Quantum theory of a nematic Fermi fluid,” *Phys. Rev. B* **64**, 195109 (2001).
- [49] Igor Khavkine, Chung-Hou Chung, Vadim Oganesyan, and Hae-Young Kee, “Formation of an electronic nematic phase in interacting fermion systems,” *Phys. Rev. B* **70**, 155110 (2004).
- [50] Hae-Young Kee and Yong Baek Kim, “Itinerant metamagnetism induced by electronic nematic order,” *Phys. Rev. B* **71**, 184402 (2005).
- [51] Eduardo Fradkin, Steven A. Kivelson, and Vadim Oganesyan, “Electron nematic phase in a transition metal oxide,” *Science* **315**, 196–197 (2007).
- [52] Chen Fang, Hong Yao, Wei-Feng Tsai, JiangPing Hu, and Steven A. Kivelson, “Theory of electron nematic order in LaFeAsO ,” *Phys. Rev. B* **77**, 224509 (2008).
- [53] Eduardo Fradkin, Steven A. Kivelson, Michael J. Lawler, James P. Eisenstein, and Andrew P. Mackenzie, “Nematic Fermi fluids in condensed matter physics,” *Annu. Rev. Condens. Matter Phys.* **1**, 153–178 (2010).
- [54] Jianhui Zhou, Wen-Yu Shan, and Di Xiao, “Spin responses and effective Hamiltonian for the two-dimensional electron gas at the oxide interface $\text{LaAlO}_3/\text{SrTiO}_3$,” *Phys. Rev. B* **91**, 241302 (2015).
- [55] Mark H. Fischer, Srinivas Raghu, and Eun-Ah Kim, “Spin-orbit coupling in $\text{LaAlO}_3/\text{SrTiO}_3$ interfaces: magnetism and orbital ordering,” *New Journal of Physics* **15**, 023022 (2013).
- [56] Xiaopeng Li, W. Vincent Liu, and Leon Balents, “Spirals and Skyrmions in Two Dimensional Oxide Heterostructures,” *Phys. Rev. Lett.* **112**, 067202 (2014).
- [57] S. Graser, T. A. Maier, P. J. Hirschfeld, and D. J. Scalapino, “Near-degeneracy of several pairing channels in multiorbital models for the Fe pnictides,” *New J. Phys.* **11**, 025016 (2009).
- [58] See supplemental material for: (i) details of RPA calculations at different densities, (ii) the form and impact of Rashba SOC, (iii) details of mean field calculations, and (iv) transport nematicity within a Drude-type model.
- [59] Gia-Wei Chern, Rafael M. Fernandes, Rahul Nandkishore, and Andrey V. Chubukov, “Broken translational symmetry in an emergent paramagnetic phase of graphene,” *Phys. Rev. B* **86**, 115443 (2012).
- [60] Rahul Nandkishore, Gia-Wei Chern, and Andrey V. Chubukov, “Itinerant Half-Metal Spin-Density-Wave State on the Hexagonal Lattice,” *Phys. Rev. Lett.* **108**, 227204 (2012).
- [61] Ivar Martin and C. D. Batista, “Itinerant Electron-Driven Chiral Magnetic Ordering and Spontaneous Quantum Hall Effect in Triangular Lattice Models,” *Phys. Rev. Lett.* **101**, 156402 (2008).
- [62] Yasuyuki Kato, Ivar Martin, and C. D. Batista, “Stability of the Spontaneous Quantum Hall State in the Triangular Kondo-Lattice Model,” *Phys. Rev. Lett.* **105**, 266405 (2010).
- [63] F. Y. Wu, “The Potts model,” *Rev. Mod. Phys.* **54**, 235–268 (1982).
- [64] Laimei Nie, Gilles Tarjus, and Steven Allan Kivelson, “Quenched disorder and vestigial nematicity in the pseudogap regime of the cuprates,” *Proceedings of the National Academy of Sciences* **111**, 7980–7985 (2014).
- [65] R. A. Borzi, S. A. Grigera, J. Farrell, R. S. Perry, S. J. S. Lister, S. L. Lee, D. A. Tennant, Y. Maeno, and A. P. Mackenzie, “Formation of a Nematic Fluid at High Fields in $\text{Sr}_3\text{Ru}_2\text{O}_7$,” *Science* **315**, 214–217 (2007).
- [66] C. Lester, S. Ramos, R. S. Perry, T. P. Croft, R. I. Bewley, T. Guidi, P. Manuel, D. D. Khalyavin, E. M. Forgan, and S. M. Hayden, “Field-tunable spin-density-wave phases in $\text{Sr}_3\text{Ru}_2\text{O}_7$,” *Nat Mater* **14**, 373–378 (2015).
- [67] Eduardo Fradkin, Steven A. Kivelson, Efstratios Manousakis, and Kwangsik Nho, “Nematic phase of the two-dimensional electron gas in a magnetic field,” *Phys. Rev. Lett.* **84**, 1982–1985 (2000).
- [68] S. Basak and E. W. Carlson, “Distinguishing XY from Ising Electron Nematics,” *ArXiv e-prints* (2017), arXiv:1704.07527 [cond-mat.str-el].
- [69] Jin-Hong Park, Choong H. Kim, Hyun-Woo Lee, and Jung Hoon Han, “Orbital chirality and Rashba interaction in magnetic bands,” *Phys. Rev. B* **87**, 041301 (2013).
- [70] Jin-Hong Park, Choong H. Kim, Jun-Won Rhim, and Jung Hoon Han, “Orbital Rashba effect and its detection by circular dichroism angle-resolved photoemission spectroscopy,” *Phys. Rev. B* **85**, 195401 (2012).
- [71] Seung Ryong Park, Choong H. Kim, Jaejun Yu, Jung Hoon Han, and Changyoung Kim, “Orbital-Angular-Momentum Based Origin of Rashba-Type Surface Band Splitting,” *Phys. Rev. Lett.* **107**, 156803 (2011).
- [72] Maria N. Gastiasoro, I. Paul, Y. Wang, P. J. Hirschfeld, and Brian M. Andersen, “Emergent defect states as a source of resistivity anisotropy in the nematic phase of iron pnictides,” *Phys. Rev. Lett.* **113**, 127001 (2014).

SUPPLEMENTAL MATERIAL

Details of RPA calculation

The bare susceptibility, which is the building block of the RPA approximations, can be written in terms of the single particle Green's functions as

$$(\chi_0(\mathbf{q}, \Omega))_{\ell_1 \ell_2; \ell_3 \ell_4} = \frac{1}{N\beta} \sum_{\mathbf{k}, \omega_n} G_{\ell_2 \ell_3}(\mathbf{k}, \omega_n) G_{\ell_4 \ell_1}(\mathbf{k} + \mathbf{q}, \omega_n + \Omega) \quad (10)$$

Given the unitary matrix $\underline{u}(\mathbf{k})$ which diagonalizes $\underline{h}(\mathbf{k})$, and its eigenvalues $\varepsilon_m(\mathbf{k})$, the Green function is

$$G_{\ell \ell'}(\mathbf{k}, \omega_n) = \sum_{m=1}^3 \frac{u_{\ell m}(\mathbf{k}) u_{\ell' m}^*(\mathbf{k})}{i\omega_n - \varepsilon_m(\mathbf{k}) + \mu}. \quad (11)$$

Using this we compute the RPA response $\underline{\chi}_{RPA}^{(c,s)}(\mathbf{q}, \Omega) = \underline{\chi}_0(\mathbf{q}, \Omega) (1 - \underline{U}^{(c,s)} \underline{\chi}_0(\mathbf{q}, \Omega))^{-1}$. In order to understand the instabilities, it suffices to focus on the matrix product $\underline{U}^{(c,s)} \underline{\chi}_0(\mathbf{q}, \Omega = 0)$; if its eigenvalues exceed unity, it signals an RPA instability. The RPA results for different electron densities are presented in figure 3. In the small J regime and for small densities, the leading instability is a $2k_F$ instability in the spin channel in the $\Gamma \rightarrow M$ direction, which is commensurate for specific densities and incommensurate in general. The $\bar{n} = 0.3$ electrons per site is an example of a commensurate order, which we study in the main text using a 2×2 unit cell. For larger densities, when $2k_F$ exceeds the length of the reciprocal lattice vectors, the ordering wavevector moves to the $M \rightarrow K$ direction. When Hund's coupling is large, we get a FM transition corresponding to a leading instability at the Γ point.

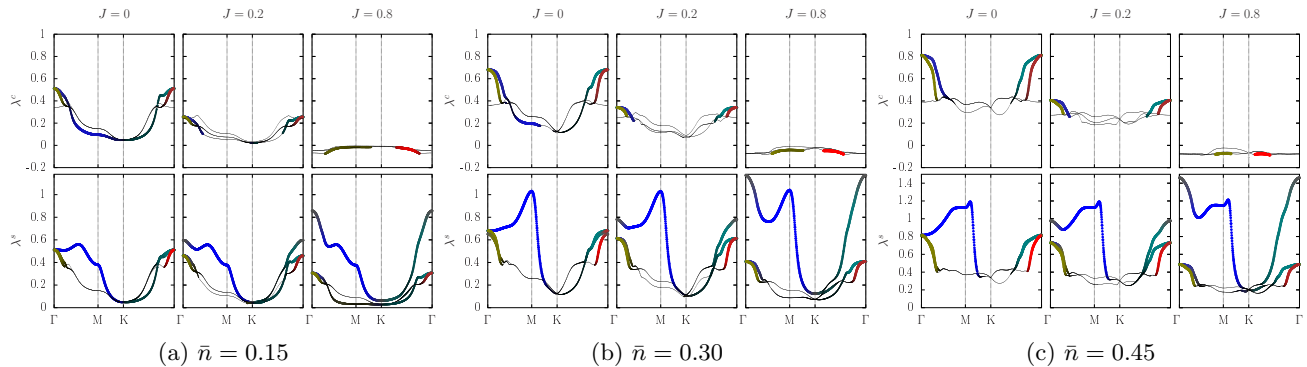


FIG. 3: Dominant three eigenvalues $\lambda^{(c,s)}$ (c =charge, s =spin) of the matrix product $\underline{U}^{(c,s)} \underline{\chi}_0(\mathbf{q}, \Omega = 0)$ for densities (a) $\bar{n} = 0.15$, (b) $\bar{n} = 0.30$, and (c) $\bar{n} = 0.45$ and indicated Hund's coupling. The color indicates the orbital content: red= xy , green= xz , blue= yz .

Spin-orbit coupling

Surface and interface 2DEGs are subject to Rashba spin-orbit coupling (SOC). This arises from a combination of inversion symmetry breaking at the interface, combined with atomic SOC.[1–3] The inversion breaking term is odd under $\mathbf{k} \rightarrow -\mathbf{k}$, and can be phenomenologically incorporated by allowing for inter-orbital hoppings which are ordinarily forbidden by the presence of inversion symmetry. Such terms have been labelled ‘orbital Rashba’ terms.[1–3] For example, an electron in the xy orbital could not move to a yz orbital along the \hat{a} direction if inversion symmetry is not broken. However, the broken symmetry at the interface will distort the orbital cloud, leading to an inter-orbital overlap which will be either stronger or weaker depending on the hopping direction (e.g.,

an $xy \rightarrow yz$ hopping is strong in the $-\hat{a}$ direction but weak in the $+\hat{a}$ direction), giving rise to inter-orbital hopping terms $\propto \sin(\mathbf{k} \cdot \mathbf{r})$. When combined with atomic SOC, this leads to the Rashba effect which has been shown to play a role in (001) oxide 2DEGs. Here, we generalize this idea to the (111) 2DEG.

Explicitly, for the (111) 2DEG in momentum space, we get for the inversion breaking ‘orbital Rashba’ term $H_{OR} = \sum_{\mathbf{k}, \ell \ell', \sigma} c_{\ell \sigma}^\dagger(\mathbf{k}) h_{\ell \ell'}^R(\mathbf{k}) c_{\ell' \sigma}(\mathbf{k})$, where

$$h^R(\mathbf{k}) = 2i\lambda_{OR} \begin{pmatrix} 0 & \sin(k_b) - \sin(k_c) & \sin(k_a) + \sin(k_c) \\ \sin(k_c) - \sin(k_b) & 0 & \sin(k_b) - \sin(k_a) \\ -\sin(k_a) - \sin(k_c) & \sin(k_a) - \sin(k_b) & 0 \end{pmatrix} \quad (12)$$

and $\ell \equiv (yz, zx, xy)$. Atomic spin-orbit coupling takes the form $H_A = -\lambda_A \vec{L} \cdot \vec{S}$ with $\lambda_A \approx 20$ meV (see e.g., Ref.4). In the $(c_{yz, \uparrow}, c_{zx, \uparrow}, \dots, c_{xy, \downarrow})^T$ basis, we can write this as $H_A = i\frac{\lambda_A}{2} \sum_{\mathbf{k}} \varepsilon_{\ell mn} \tau_{\sigma \sigma'}^n c_{\ell \sigma}^\dagger(\mathbf{k}) c_{m \sigma'}(\mathbf{k})$, where $\varepsilon_{\ell mn}$ is the Levi-Civita symbol and τ^n the Pauli matrices.

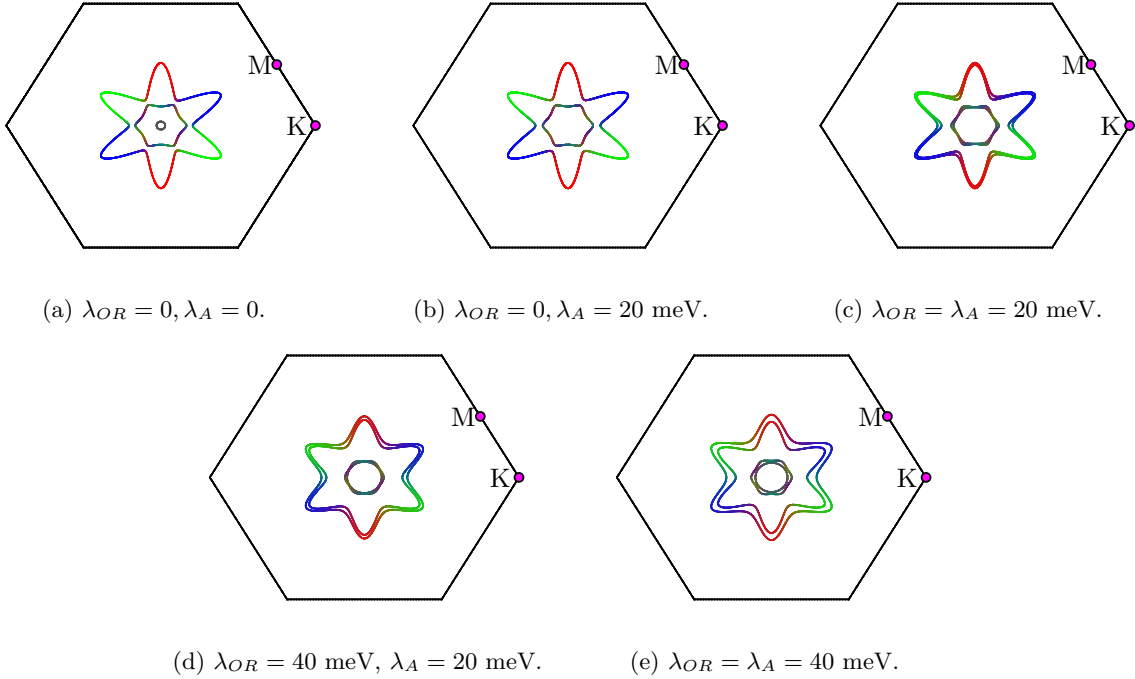


FIG. 4: Fermi surfaces for different strengths of orbital Rashba λ_{OR} coupling and atomic SOC λ_A at $\bar{n} = 0.3$.

What is the impact of such atomic SOC and inversion breaking on the Fermi surface? Comparing figure 4a ($\lambda_A = 0, \lambda_{OR} = 0$) to figure 4b ($\lambda_A = 20$ meV, $\lambda_{OR} = 0$) we see that the main effect of atomic spin-orbit coupling on the Fermi surface is the disappearance of the small band near the Γ point, which gets pushed below the Fermi level. The leading magnetic instability uncovered in our RPA (reported in the main text and above) occurs at the wavevector connecting the tips of the elliptical Fermi surfaces. Near these tips, we find that the Fermi surface is nearly unaffected which we can understand since the Fermi surface near these regions is almost entirely composed of a single orbital. Using $\lambda_A = \lambda_{OR} = 20$ meV (see Ref.4), we obtain the Fermi surface shown in figure 4c. We can see that the Rashba spin-orbit coupling breaks the spin degeneracy, previously protected by inversion and time-reversal symmetry. The tips of ellipses are once again nearly unaffected by this term, the main changes to Fermi surfaces being in the $\Gamma \rightarrow K$ direction where the different orbitals tend to strongly hybridize. However, even here the changes are small. We include figures 4d and 4e to show the effect of even larger inversion breaking on the Fermi surfaces; however we point out that these Fermi surfaces are not consistent with ARPES data on the STO surface 2DEG, suggesting that they are too large to be of relevance.

Details of the MFT calculation

The mean field theory can be cast in the form of a variational minimization where we pick the variational state to be the ground state of a variational Hamiltonian $H_{\text{var}} = H_0 - \sum_{i\ell}(\phi_{i\ell} + \mu)n_{i\ell} - \sum_{i\ell} \mathbf{b}_{i\ell} \cdot \mathbf{S}_{i\ell}$, with $\{\phi_{i\ell}, \mathbf{b}_{i\ell}\}$ being variational parameters which allow in general for site and orbital dependent order parameters. The expression for the variational free energy is given by:

$$\mathcal{F}_{\text{var}} = \sum_{i\ell\ell'} \left\{ \langle n_{i,\ell} \rangle \langle n_{i,\ell'} \rangle \left[\frac{U}{4} \delta_{\ell\ell'} + \frac{1}{2} \left(U - \frac{5}{2} J \right) (1 - \delta_{\ell\ell'}) \right] - \langle \mathbf{S}_{i,\ell} \rangle \cdot \langle \mathbf{S}_{i,\ell'} \rangle [U \delta_{\ell\ell'} + J(1 - \delta_{\ell\ell'})] \right\} \\ + \int_{FBZ} (d^2\mathbf{k}) \text{Tr}(\underline{u}^\dagger(\mathbf{k}) \underline{h}(\mathbf{k}) \underline{u}(\mathbf{k}) \underline{n}_F(\mathbf{k})) - TS \quad (13)$$

where $\underline{u}(\mathbf{k})$ is the matrix which diagonalizes H_{var} , \underline{n}_F is the Fermi-Dirac distribution, and the thermal expectation values $\langle \cdot \rangle$ are taken with respect to the equilibrium density matrix of the variational Hamiltonian, i.e., $e^{-H_{\text{var}}/T}$, and S is the fermion entropy for given field configuration $\phi_{i\ell}$ and $\mathbf{b}_{i\ell}$.

We discuss two cases in the main text, a single- \mathbf{Q} spiral mean field theory which can be formulated directly in momentum space with a single site unit cell, and a case where we study broken symmetry states with 2×2 real space unit cell which allows us to also explore multi- \mathbf{Q} order parameters for the commensurate AF.

Spiral MFT (zero temperature)

The $T = 0$ spiral mean field theory is performed with only intra-orbital orders, uniform density and spiral magnetization with fixed wavevector \mathbf{q} , so $\langle n_{i\ell\sigma} \rangle = \frac{1}{2} \rho_\ell$, and $\langle S_{i\ell}^\pm \rangle = m_\ell e^{\pm i\mathbf{q} \cdot \mathbf{r}_i}$. This leads to the effective Hamiltonian

$$H_{\text{spiral}} = \sum_{\mathbf{k}} \Psi^\dagger(\mathbf{k}) \mathcal{H}(\mathbf{k}) \Psi(\mathbf{k}) \quad (14)$$

where $\Psi^\dagger(\mathbf{k}) \equiv (c_{yz,\uparrow}^\dagger(\mathbf{k}), c_{zx,\uparrow}^\dagger(\mathbf{k}), c_{xy,\uparrow}^\dagger(\mathbf{k}), c_{yz,\downarrow}^\dagger(\mathbf{k} + \mathbf{q}), c_{zx,\downarrow}^\dagger(\mathbf{k} + \mathbf{q}), c_{xy,\downarrow}^\dagger(\mathbf{k} + \mathbf{q}))^T$, and

$$\mathcal{H}(\mathbf{k}) = \begin{pmatrix} \varepsilon_{\mathbf{k}}^{yz} & \gamma_{\mathbf{k}}^{yz,zx} & \gamma_{\mathbf{k}}^{yz,xy} & \zeta_{yz} & 0 & 0 \\ \gamma_{\mathbf{k}}^{yz,zx*} & \varepsilon_{\mathbf{k}}^{zx} & \gamma_{\mathbf{k}}^{zx,xy} & 0 & \zeta_{zx} & 0 \\ \gamma_{\mathbf{k}}^{yz,xy*} & \gamma_{\mathbf{k}}^{zx,xy*} & \varepsilon_{\mathbf{k}}^{xy} & 0 & 0 & \zeta_{xy} \\ \zeta_{yz} & 0 & 0 & \varepsilon_{\mathbf{k}+\mathbf{q}}^{yz} & \gamma_{\mathbf{k}+\mathbf{q}}^{yz,zx} & \gamma_{\mathbf{k}+\mathbf{q}}^{yz,xy} \\ 0 & \zeta_{zx} & 0 & \gamma_{\mathbf{k}+\mathbf{q}}^{yz,zx*} & \varepsilon_{\mathbf{k}+\mathbf{q}}^{zx} & \gamma_{\mathbf{k}+\mathbf{q}}^{zx,xy} \\ 0 & 0 & \zeta_{xy} & \gamma_{\mathbf{k}+\mathbf{q}}^{yz,xy*} & \gamma_{\mathbf{k}+\mathbf{q}}^{zx,xy*} & \varepsilon_{\mathbf{k}+\mathbf{q}}^{xy} \end{pmatrix} \quad (15)$$

Here

$$\varepsilon_{\mathbf{k}}^\ell = (\varepsilon_{\mathbf{k}}^{\ell(0)} - \mu) + \frac{U}{2} \rho_\ell + (U - \frac{5}{2} J) \sum_{\ell \neq \ell'} \rho_{\ell'} \quad (16)$$

$$\zeta_\ell = -U m_\ell - J \sum_{\ell \neq \ell'} m_{\ell'} \quad (17)$$

with $\varepsilon_{\mathbf{k}}^{\ell(0)}$ being the bare intra-orbital dispersion for orbital ℓ , and $\gamma_{\mathbf{k}}$ being inter-orbital hybridization. Using expression (13), we compute the energy for various \mathbf{q} and pick the wavevector which minimizes the energy. This leads us to the phase diagrams shown in Figs. 2(a-c) of the main text.

MFT with 2×2 real space unit cell

For the 2×2 unit cell, the most general \mathbf{b} field can be expressed in terms of 4 vector parameters \mathbf{b}_α ($\alpha = 0, 1, 2, 3$),

$$\mathbf{b}_{i\ell} = \mathbf{b}_0 + \mathbf{b}_1 (-1)^{m+n} \delta_{\ell,yz} + \mathbf{b}_2 (-1)^m \delta_{\ell,zx} + \mathbf{b}_3 (-1)^n \delta_{\ell,xy} \quad (18)$$

where (m, n) correspond to lattice coordinates of site i along the \hat{a} and \hat{c} directions respectively. We thus formulate this mean field theory partly in momentum space where we work in the corresponding reduced BZ. The paramagnetic state corresponds to $\mathbf{b}_\alpha = 0$ for all α , and the ferromagnetic state to only $\mathbf{b}_0 \neq 0$. The different AF states all correspond to $\mathbf{b}_0 = 0$ and different nonzero \mathbf{b}_α (for $\alpha \neq 0$). The collinear AF-1 (or AF-2 or AF-3) state are obtained when respectively only a single component of one (or two or three) \mathbf{b}_α is nonzero. The orthogonal AF-2 (or AF-3) corresponds to two (three) orthogonal choices of nonzero \mathbf{b}_α fields. Minimizing the free energy, we are led to the phase diagram shown in Fig. 2(d) of the main text.

As seen from the figure, there are large regimes where we find robust AF-1 and FM phases. We also find smaller regimes where AF-2 and AF-3 phases are stabilized which involved the superposition of two or three \mathbf{Q} orders, but the free energy per site for these states is lower than the AF-1 state by a very small amount (of order $\sim 10^{-5}t$). Furthermore, the free energy difference per site between different superpositions (collinear, coplanar, orthogonal) in the multi- \mathbf{Q} states (AF-2, AF-3) are even smaller, $\sim 10^{-7}t$.

We have studied the temperature dependence of a few points in the AF phases and found that as the temperature is raised, the AF-2 and AF-3 become an AF-1 phase, consistent with [5]. The mean field critical temperature into the PM starting significantly deep in the AF and FM phases is $\simeq 0.18t$; without SOC, this will be suppressed to zero, leaving only vestigial orbital and nematic orders. A numerical study of the renormalized T_c for such vestigial orders taking full thermal fluctuations into account will be discussed elsewhere.

Nematicity in the Drude conductivity

Simple Drude-like considerations are enough to determine how the electric conductivity depends on the nematic order parameter ψ_n . We begin by assuming that only ψ_n has condensed and that there is no magnetic order. For simplicity, we further assume that the inter-orbital hopping is zero. Thus, each orbital, denoted by its preferred hopping direction, $\ell = a(xy), b(xz), c(yz)$, has a separate contribution to the conductivity tensor, $\hat{\sigma} = \sum_\ell \hat{\sigma}_\ell$. In terms of Cartesian coordinates, x, y , used in the main text, with $\hat{a} = \hat{x}$, $\hat{b} = \hat{x}/2 + \hat{y}\sqrt{3}/2$, and $\hat{c} = -\hat{x}/2 + \hat{y}\sqrt{3}/2$, we get

$$\hat{\sigma}_a = \begin{pmatrix} \sigma_1 & 0 \\ 0 & \sigma_2 \end{pmatrix}, \quad \hat{\sigma}_b = \begin{pmatrix} \frac{1}{4}\sigma_1 + \frac{3}{4}\sigma_2 & \frac{\sqrt{3}}{4}(\sigma_1 - \sigma_2) \\ \frac{\sqrt{3}}{4}(\sigma_1 - \sigma_2) & \frac{3}{4}\sigma_1 + \frac{1}{4}\sigma_2 \end{pmatrix}, \quad \hat{\sigma}_c = \begin{pmatrix} \frac{1}{4}\sigma_1 + \frac{3}{4}\sigma_2 & -\frac{\sqrt{3}}{4}(\sigma_1 - \sigma_2) \\ -\frac{\sqrt{3}}{4}(\sigma_1 - \sigma_2) & \frac{3}{4}\sigma_1 + \frac{1}{4}\sigma_2 \end{pmatrix}, \quad (19)$$

where, in general $\sigma_1 \neq \sigma_2$. A six-fold rotation operation, C_6 , relates the tensors above: $\hat{\sigma}_b = C_6 \hat{\sigma}_a C_6^{-1}$ and $\hat{\sigma}_c = C_6^{-1} \hat{\sigma}_a C_6$. Within a Drude picture, the matrix elements are proportional to the density of electrons, in this case, for each orbital separately. Therefore, we can approximate $\hat{\sigma} \approx \sum_\ell \rho_\ell \hat{\sigma}_\ell / \rho_0$, where, ρ_ℓ is the electron density in each orbital, while the average density per orbital is denoted by ρ_0 . The nematic order parameter captures the imbalance in orbital densities, $\psi_n \sim ((\rho_a - \rho_0) + \omega(\rho_b - \rho_0) + \omega^*(\rho_c - \rho_0)) / \rho_0$. Putting everything together, we find

$$\hat{\sigma} \approx \frac{3}{2}(\sigma_1 + \sigma_2) \begin{pmatrix} 1 & 0 \\ 0 & 1 \end{pmatrix} + \frac{1}{2}(\sigma_1 - \sigma_2) \begin{pmatrix} \text{Re } \psi_n & \text{Im } \psi_n \\ \text{Im } \psi_n & -\text{Re } \psi_n \end{pmatrix}. \quad (20)$$

Finally, assuming ψ_n is small, one can obtain a qualitatively similar dependence of the resistivity tensor $\hat{\rho}$ on ψ_n .

[1] Seung Ryong Park, Choong H. Kim, Jaejun Yu, Jung Hoon Han, and Changyoung Kim, ‘‘Orbital-Angular-Momentum Based Origin of Rashba-Type Surface Band Splitting,’’ *Phys. Rev. Lett.* **107**, 156803 (2011).

[2] Jin-Hong Park, Choong H. Kim, Jun-Won Rhim, and Jung Hoon Han, ‘‘Orbital Rashba effect and its detec-

tion by circular dichroism angle-resolved photoemission spectroscopy,’’ *Phys. Rev. B* **85**, 195401 (2012).

[3] Jin-Hong Park, Choong H. Kim, Hyun-Woo Lee, and Jung Hoon Han, ‘‘Orbital chirality and Rashba interaction in magnetic bands,’’ *Phys. Rev. B* **87**, 041301 (2013).

[4] Zhicheng Zhong, Anna Tóth, and Karsten Held, ‘‘Theory of spin-orbit coupling at LaAlO₃/SrTiO₃ interfaces and SrTiO₃ surfaces,’’ *Phys. Rev. B* **87**, 161102 (2013).

[5] Rahul Nandkishore, Gia-Wei Chern, and Andrey V. Chubukov, ‘‘Itinerant Half-Metal Spin-Density-Wave

State on the Hexagonal Lattice," Phys. Rev. Lett. **108**, 227204 (2012).